

**Climatology, seasonality and trends of oceanic coherent
eddies**

Josué Martínez-Moreno¹, Andrew McC. Hogg¹, and Matthew H. England²

⁴ Research School of Earth Science and ARC Center of Excellence for Climate Extremes, Australian
⁵ National University, Canberra, Australia

⁶ Climate Change Research Centre (CCRC), UNSW Australia, Sydney NSW, Australia

Key Points:

- ⁸ Kinetic energy of coherent eddies contain around 50% of the surface ocean kinetic
⁹ energy budget.
- ¹⁰ Seasonal cycle of the number of coherent eddies and coherent eddy amplitude re-
¹¹ veal a 3-6 month lag to wind forcing
- ¹² Seasonal lag between the number of coherent eddies and eddy amplitude.
- ¹³ The coherent eddy amplitude has increase at a rate of 3 cm per decade since 1993.

14 **Abstract**

15 Ocean eddies influence regional and global climate through mixing and transport
 16 of heat and properties. One of the most recognizable and ubiquitous feature of oceanic
 17 eddies are vortices with spatial scales of tens to hundreds of kilometers, frequently re-
 18 ferred as “mesoscale eddies” or “coherent eddies”. Coherent eddies are known to trans-
 19 port properties across the ocean and to locally affect near-surface wind, cloud proper-
 20 ties and rainfall patterns. Although coherent eddies are ubiquitous, yet their climatol-
 21 ogy, seasonality and long-term temporal evolution remains poorly understood. Thus, we
 22 examine the kinetic energy contained by coherent eddies and we present the annual, in-
 23 terannual, and long-term changes of automatically identified coherent eddies from satel-
 24 lite observations from 1993 to 2018. Around 50% of the kinetic energy contained by ocean
 25 eddies corresponds to coherent eddies. Additionally, a strong hemispherical seasonal cy-
 26 cle is observed, with a 3–6 months lag between the wind forcing and the response of the
 27 coherent eddy field. Furthermore, the seasonality of the number of coherent eddies and
 28 their amplitude reveals that the number of coherent eddies responds faster to the forc-
 29 ing (~3 months), then the coherent eddy amplitude (which is lagged by ~6 months). Our
 30 analysis highlights the relative importance of the coherent eddy field in the ocean ki-
 31 netic energy budget, implies a strong response of the eddy number and eddy amplitude
 32 to forcing at different time-scales, and showcases the seasonality, and multidecadal trends
 33 of coherent eddy properties.

34 **Plain language summary**35 **1 Introduction**

36 Mesoscale ocean variability with spatial scales of tens to hundreds of kilometers is
 37 comprised of processes such as vortices, waves, and jets (Ferrari & Wunsch, 2009; Fu et
 38 al., 2010). These mesoscale processes are highly energetic, and they play a crucial role
 39 in the transport of heat, salt, momentum, and other tracers through the ocean (Wun-
 40 sch & Ferrari, 2004; Wyrtki et al., 1976; Gill et al., 1974). Possibly, the most recogniz-
 41 able and abundant process observed from satellites is mesoscale vortices. Although mesoscale
 42 vortices are commonly referred to in literature as “mesoscale eddies”, this term is also
 43 often used to describe the total mesoscale ocean variability (the time-varying component
 44 of the mesoscale flow), thus, here we will refer to mesoscale vortices as *coherent eddies*.

45 Coherent eddies are quasi-circular currents. According to their rotational direction,
46 the sea surface height anomaly within a coherent eddy can have a negative or positive
47 sea surface height anomaly (cold-core and warm-core coherent eddies, respectively). This
48 characteristic sea surface height signature of coherent eddies has been utilized to auto-
49 matically identify and track coherent eddies from satellite altimetry (Cui et al., 2020;
50 Martínez-Moreno et al., 2019; Ashkezari et al., 2016; Faghmous et al., 2015; Chelton et
51 al., 2007). Automated identification algorithms of coherent eddies have shown their ubiq-
52 uituity in the oceans, with a predominant influence at hotspots of eddy activity such as bound-
53 ary currents and the Antarctic Circumpolar Current. In these regions, Chelton et al. (2011)
54 estimated that coherent eddies contribute around 40–50% of the mesoscale kinetic en-
55 ergy (Chelton et al., 2011) and thus a significant fraction of the total kinetic energy (Fer-
56 rari & Wunsch, 2009). Although this unique estimate showcases the importance of the
57 mesoscale coherent eddy field, the energy contained by coherent eddies was estimated
58 by extracting the geostrophic velocities within the detected coherent eddies, thus it is
59 possible it may contain energy from other processes. Coherent eddies are not only abun-
60 dant and may have a large proportion of the surface kinetic energy budget, but they are
61 also essential to ocean dynamics as concluded by many previous studies (Patel et al., 2020;
62 Schubert et al., 2019; Pilo et al., 2015; Frenger et al., 2015, 2013; Beron-Vera et al., 2013;
63 Siegel et al., 2011; Hogg & Blundell, 2006).

64 There is broad consensus that mesoscale eddy kinetic energy has a pronounced sea-
65 sonal variability (Uchida et al., 2017; Kang & Curchitser, 2017; Qiu & Chen, 2004; Qiu,
66 1999). Several hypotheses have been proposed to explain this seasonality including: sea-
67 sonal variations of atmospheric forcing (Sasaki et al., 2014), seasonality of the mixed layer
68 depth (Qiu et al., 2014; Callies et al., 2015), seasonality of the intensity of barotropic in-
69 stability (Qiu & Chen, 2004), the variability of the baroclinic instability due to the sea-
70 sonality of the vertical shear (Qiu, 1999), and a seasonal lag of the inverse energy cas-
71 cade (energy is transported between scales from small to large; Arbic et al., 2013) in com-
72 bination with the presence of a front in the mixed layer, which can lead to a seasonal
73 cycle of the baroclinic instability (Qiu et al., 2014). On one hand, processes such as barotropic
74 and baroclinic instabilities control the seasonality of coherent eddies in the ocean. On
75 the other hand, recent studies using observations and eddy-permitting climate models
76 suggest several long-term adjustments of the global ocean capable of long-term changes
77 in the coherent eddy field. Such readjustments include a multidecadal increase in the ocean

stratification resulted from temperature and salinity changes (Li et al., 2020), a horizontal readjustment of the sea surface temperature gradients (Ruela et al., 2020; Bouali et al., 2017; Cane et al., 1997), and an intensification of the kinetic energy, eddy kinetic energy, and mesoscale eddy kinetic energy over the last 3 decades as a consequence of an increase in wind forcing (Hu et al., 2020; Wunsch, 2020; Martínez-Moreno et al., 2021). All these seasonal factors and long-term readjustments directly influence the annual and decadal response of the coherent eddy field, however, the seasonality of the coherent component of the eddy kinetic energy, as well as the seasonal cycle and trends of the coherent eddy statistics remain unknown.

Here we present a new global climatology of the coherent eddy kinetic energy by reconstructing the coherent eddy signature from satellite observations. Our climatology documents the seasonal cycle of the coherent eddy kinetic energy, and seasonal cycle and long-term trends of the coherent eddy properties over the satellite record. Moreover, we conduct more detail analysis in regions where coherent eddies dominate the eddy kinetic energy field. This paper is structured as follows: the data sources and methodology are described in section 2. Then, we present the climatology, energy ratios, and global seasonality of the coherent eddy kinetic energy in subsection 3. Subsection 4 presents the global climatology and seasonality of coherent eddy properties, followed by the seasonal cycle and coherent eddy property time-series in regions dominated by coherent eddies (subsection 6). We then focus our attention on the long-term changes of the coherent eddy properties (section 5). Finally, section 7 summarizes the main results and discusses the implications of this study.

2 Methods

We use daily sea surface height (SSH) data made available by the Copernicus Marine Environment Monitoring Service in near real time (CMEMS, 2017). This gridded product contains the sea surface height and geostrophic velocities with daily 0.25° resolution from January 1993 to 2019. The daily geostrophic velocities allowed us to compute the kinetic energy (KE) and eddy kinetic energy (EKE) over the satellite record. The main source of EKE is the time-varying wind (Ferrari & Wunsch, 2009), thus we computed the seasonal cycle of the wind magnitude from the JRA55 reanalysis (Japan Meteorological Agency, Japan, 2013) using wind velocities at 10m above the ocean's surface.

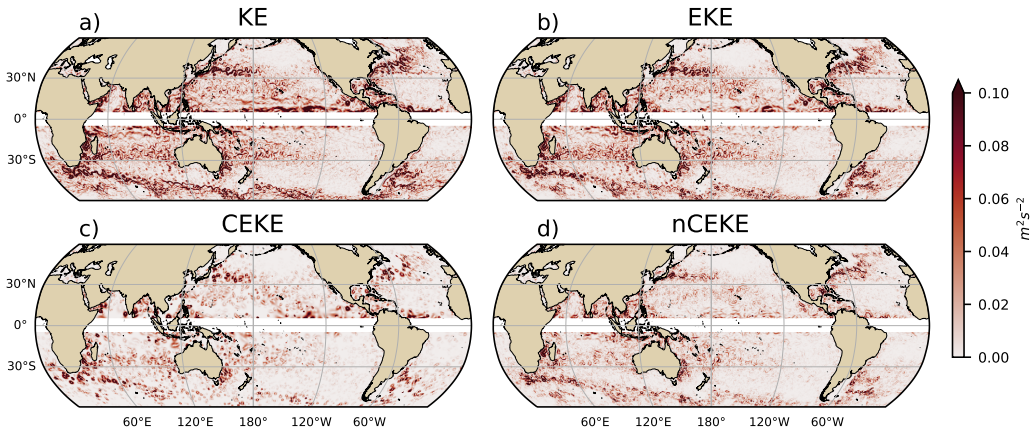
Over the same record, coherent eddy statistics from Martínez-Moreno et al. (2019), hereafter M-M, are analyzed and compared to those released by Chelton & Schlax (2013), both datasets are gridded in a 1° resolution. Although both datasets are produced via automated eddy identification algorithms using closed contours of SSH, these datasets have important differences in the criteria they use to identify and record coherent eddies statistics. The major difference include; (i) M-M's algorithm requires an adjustment between a 2D Gaussian and the SSH anomaly (SSHa) surface within the identify closed contour, while Chelton's only uses the outer-most closed contour of SSH; (ii) M-M's dataset reports the maximum SSHa within the identified coherent eddy, while Chelton's algorithm reports the maximum SSH value minus the discrete level in which the coherent eddy was identified; M-M's dataset includes all detected coherent eddies, while Chelton's dataset excludes (iii) coherent eddies with lifetimes shorter than four weeks and (iv) coherent eddy amplitudes smaller than 1cm. Moreover, M-M's algorithm allows the reconstruction of the coherent eddy field under the assumption that coherent eddies have a 2D Gaussian imprint in the sea surface height. These Gaussian anomalies then allow us to estimate the coherent geostrophic eddy velocities and thus the kinetic energy contained only by coherent eddies.

2.1 Kinetic Energy decomposition

Kinetic energy is commonly divided into the mean and time-varying components through a Reynolds decomposition. At a given time, the velocity field $\mathbf{u} = (u, v)$ is split into the time mean ($\bar{\mathbf{u}}$) and time varying components (\mathbf{u}'). Moreover, M-M proposed to further decompose the eddy kinetic energy into the energy contained by coherent features (\mathbf{u}'_e) and non-coherent features (\mathbf{u}'_n). Therefore the KE equation can be written as:

$$\text{KE} = \underbrace{\bar{u}^2 + \bar{v}^2}_{\text{MKE}} + \underbrace{u'^2_e + v'^2_e + u'^2_n + v'^2_n}_{\text{CEKE}} + \underbrace{\mathcal{O}_c^2 + \mathcal{O}^2}_{\text{nCEKE}} \quad (1)$$

Due to the properties of this decomposition, the second order term \mathcal{O}^2 is zero when averaged over the same period as $\bar{\mathbf{u}}$. However, \mathcal{O}_c^2 is negligible when averaged over time and space. More information about the decomposition of the field into coherent features and non-coherent features is explained by Martínez-Moreno et al. (2019). A global snap-



143 **Figure 1.** Snapshot of surface kinetic energy (\overline{KE}), surface eddy kinetic energy (\overline{EKE}),
 144 surface coherent eddy kinetic energy (\overline{CEKE}), and surface non-coherent eddy kinetic energy
 145 (\overline{nCEKE}) for the 1st of January 2017.

138 shot of each component of kinetic energy decomposition is shown in figure 1, where the
 139 KE and EKE are comprised of rings and filaments. As expected, the decomposition of
 140 EKE into CEKE and nCEKE components exhibit only ring-like signatures expected of
 141 coherent eddies, while the non-coherent component shows filaments and some uniden-
 142 tified coherent eddies.

146 2.2 Eddy statistics

147 The eddy statistics used in this study include the eddy count ($cEddy_n$) defined as
 148 the number of eddies per grid cell, and the mean eddy amplitude defined as the mean
 149 amplitude of the coherent eddies within the cell ($cEddy_{amp}$). The latter metric can be
 150 separated into positive ($cEddy_{amp}^+$) and negative ($cEddy_{amp}^-$) coherent eddy amplitudes,
 151 defined as the mean amplitude of warm core and cold core coherent eddies, respectively,
 152 within the cell. The absolute eddy amplitude ($|cEddy_{amp}|$) is then defined as:

$$|cEddy_{amp}| = \frac{1}{2} (cEddy_{amp}^+ - cEddy_{amp}^-) \quad (2)$$

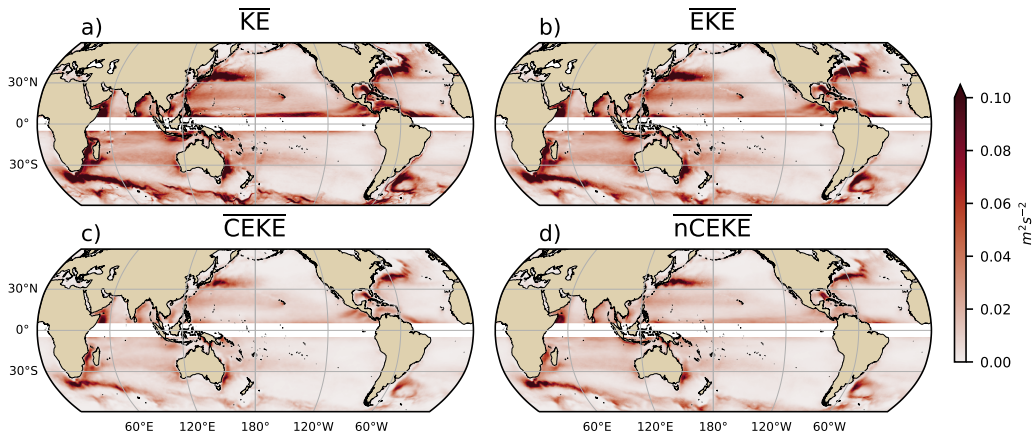
153 Note that the $cEddy_{amp}^+$ and $cEddy_{amp}^-$ are sign definite, thus the difference will always
 154 be positive, mean $cEddy_{amp}$ can be negative or positive noting the dominant polarity
 155 of coherent eddies in the region. We analyze the climatology, seasonal cycles and trends
 156 of the eddy statistics between 1993 and 2019. We exclude the equatorial region ($10^\circ S$
 157 - $10^\circ N$) and poleward of 60° . Note that the climatology of $cEddy_n$ is computed by adding

158 all the identified eddies over the record, while all other climatological statistics are com-
 159 puted as the time-average over the record. Seasonal climatologies are calculated for the
 160 monthly average of each coherent eddy statistic, while hemispherical time-series are fil-
 161 tered with a running average of 90 days. Trends of $cEddy_n$ and $|cEddy_{amp}|$ are calcu-
 162 lated by coarsening the dataset to a 5° grid, and then linear trends are computed for each
 163 grid point, the statistical significance is assessed by a modified Mann-Kendall test (Yue
 164 & Wang, 2004). Time averages are denoted by $\overline{\cdot}$, while area averages are shown by $\langle \cdot \rangle$.

165 3 Global Coherent Eddy Energetics

166 The climatology geostrophic components of the kinetic energy decomposition es-
 167 timated from sea surface height are shown in Figure 2. These maps show that many re-
 168 gions of the global ocean are highly energetic in mean KE (\overline{KE}), mean EKE (\overline{EKE}), mean
 169 coherent eddy kinetic energy (\overline{CEKE}) and mean non-coherent eddy kinetic energy (\overline{nCEKE}).
 170 The spatial pattern highlights well known regions of the ocean, where mesoscale processes
 171 are abundant, such is the case of western boundary currents, the Antarctic Circumpo-
 172 lar Current and regions within the ocean gyres. Remarkably, the spatial distribution of
 173 the energy contained by the reconstructed mesoscale coherent eddies and non-coherent
 174 components are similar (Figures 2c,d), which can be thought as regions where mesoscale
 175 activity is intense, however, there are some regions where coherent eddies dominate over
 176 non-coherent and vice-versa. Overall, this decomposition suggest that boundary currents
 177 and other energetic regions, in particularly, eddy-rich regions in the ocean contain both
 178 coherent and non-coherent components of the kinetic energy.

182 Eddy kinetic energy is known to be more than an order of magnitude greater than
 183 MKE (Gill et al., 1974), this is clearly shown in Figure 3a, where the ratio of \overline{EKE} is re-
 184 sponsible of almost all the \overline{KE} across the ocean, except for regions with persistent cur-
 185 rents over time. Such regions are located in the mean boundary current locations, the
 186 equatorial pacific currents and regions in the Antarctic Circumpolar current, where the
 187 EKE explains around 40% of the \overline{KE} . As estimated by a previous study by Chelton et
 188 al. (2011), the EKE within coherent eddies with lifetimes grater than 4 weeks contain
 189 between 40 to 60 percent of the \overline{EKE} . Our result from reconstructing the coherent eddy
 190 signature (Figure 3b) further corroborates that the coherent component (\overline{CEKE}) has around
 191 50% of the \overline{KE} (Figure 3d). Furthermore, global averages of the ratios show \overline{EKE} ex-
 192 plains approximately 78% of the ocean *MKE* field, while non coherent eddy features con-

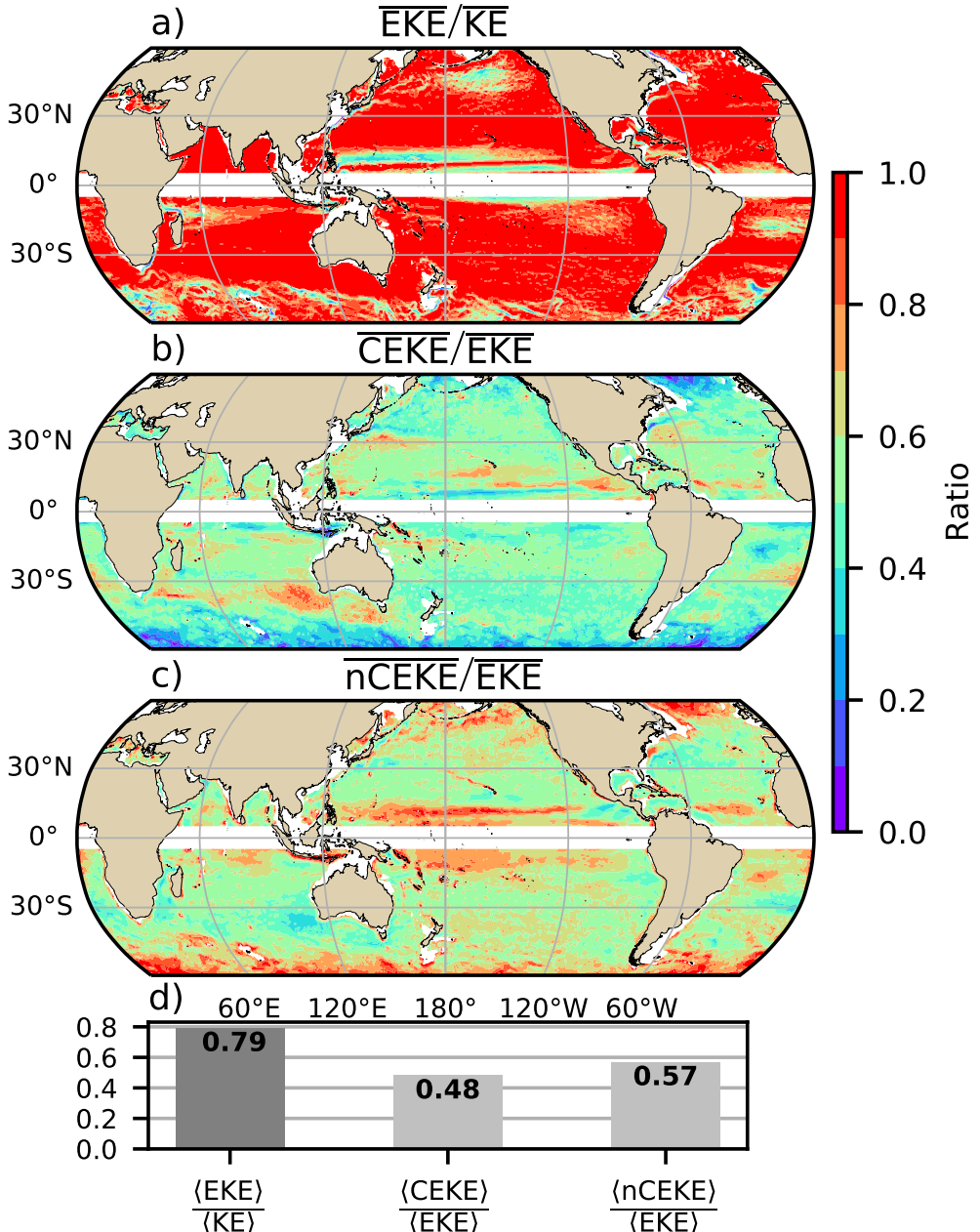


179 **Figure 2.** Climatology of surface kinetic energy (\overline{KE}), surface eddy kinetic energy (\overline{EKE}),
 180 surface coherent eddy kinetic energy (\overline{CEKE}), and surface non-coherent eddy kinetic energy
 181 (\overline{nCEKE}) between 1993-2018.

193 tain 48% and 57% percent. Note the globally averaged coherent and non coherent com-
 194 ponents do not add to 100% as the cross terms (\mathcal{O}_c^2) are different to zero. This is likely
 195 to errors in the coherent eddy reconstruction. The spatial pattern reveals a dominance
 196 of the \overline{CEKE} equatorward from the boundary currents and areas with large coherent eddy
 197 contributions of around 90% of the region's eddy kinetic energy, for example, south of
 198 Australia, Tehuantepec Gulf and South Atlantic. An evident signal is an reduction of
 199 the energy contained by coherent eddies at high latitudes and an increase in the energy
 200 explained by non-coherent eddies, this could be a consequence of the incapability of the
 201 0.25° satellite resolution (~ 13 km at 60°) to fully resolve coherent eddies with scales
 202 smaller than ~ 10 km (first baroclinic Rossby radius at 60°)

212 3.0.1 Seasonality

213 In accordance with the previously observed EKE seasonal cycle, we investigate sea-
 214 sonal cycle of the EKE and CEKE for the northern hemisphere (NH; $10^\circ N - 60^\circ N$) and
 215 Southern Hemisphere (SH; $60^\circ S - 10^\circ S$). In both hemispheres (Figure 4), the EKE and
 216 CEKE peak during the hemispherical summer. In the northern hemisphere, the largest
 217 EKE and CEKE occurs ~ 6 months after the maximum winds (Figure 4c and d), while
 218 the Southern ocean seems to respond within ~ 4 months (Figure 4g, and h). This sea-
 219 sonal lag and maximum is consistent with a time-lag of the inverse cascade (Sasaki et



203 **Figure 3.** Ratios of the kinetic energy components. a) Map of the proportion of mean eddy
 204 kinetic energy (EKE) versus mean kinetic energy (\bar{KE}); b) Map of the percentage of mean co-
 205 herent eddy kinetic energy (\overline{CEKE}) versus mean eddy kinetic energy (\overline{EKE}); c) Map of the
 206 percentage of mean non-coherent eddy kinetic energy (\overline{nCEKE}) versus mean eddy kinetic energy
 207 (\overline{EKE}); d) Global averaged percentage of mean eddy kinetic energy ($\langle EKE \rangle$) versus the global
 208 mean kinetic energy ($\langle \bar{KE} \rangle$), and percentage of mean coherent eddy kinetic energy ($\langle \overline{CEKE} \rangle$)
 209 and mean non coherent eddy kinetic energy ($\langle \overline{nCEKE} \rangle$) versus global mean eddy kinetic energy
 210 ($\langle \overline{EKE} \rangle$). Regions where the depth of the ocean is shallower than 1000m are removed from the
 211 ratio estimation.

220 al., 2014; Qiu et al., 2014) where winter has the highest energy at the smallest scales (non-
 221 solvable with satellite observations), spring and autumn have the highest and lowest en-
 222 ergy in scales of 50-100 km, and summertime has the highest energy at the largest scales
 223 (> 100 km; Uchida et al. 2017), thus the maximum of EKE and CEKE located during
 224 summertime suggest eddies and coherent eddies have scales larger than 100 km.

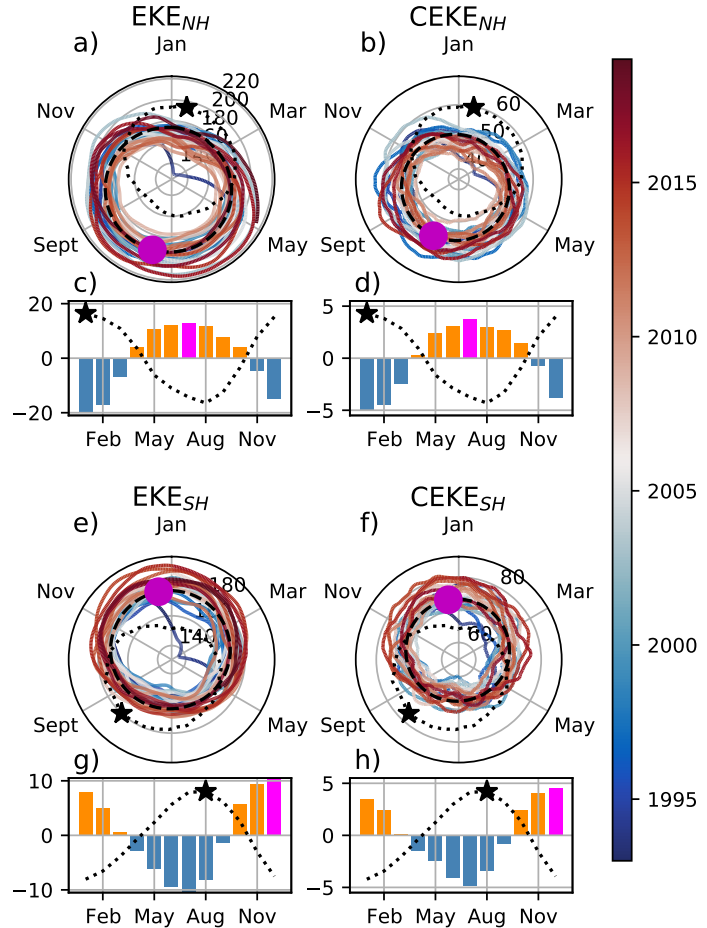
225 The cyclic plots in Figure 4 shows the temporal evolution of EKE and CEKE. Note
 226 that high frequency variability can be observed in the CEKE field with temporal scales
 227 of a few months, this could be attributed local dynamics averaged over the hemisphere,
 228 as well as errors within the coherent eddy identification. Additionally, cyclic plots high-
 229 light long-term temporal changes over the record; (i) northern hemisphere winters show
 230 a decrease in the CEKE field and (ii) the Southern hemisphere show concentric growth
 231 over time in EKE and CEKE, which support the increasing trends in the Southern Ocean
 232 observed by (Hogg et al., 2015; Martínez-Moreno et al., 2019; Martínez-Moreno et al.,
 233 2021).

240 4 Global Coherent Eddy Statistics

241 Identified coherent eddies properties using automated algorithms allows to estimate
 242 the contribution of changes in the number of eddies and the eddy amplitude.

243 Figure 5

- 244 • A comparison with previous identified numbers show a consistent pattern in the
 245 eddy count. The difference in the magnitude could be a consequence of Chelton
 246 et al. (2007) filtering the coherent eddies with lifespans longer than 16 weeks.
- 247 • Both datasets show a large number of eddies in the East North Pacific, East North
 248 Atlantic, as well as the East South Pacific, East South Atlantic and East Indian
 249 Ocean.
- 250 • While the number of eddies detected in the tropics is quite small.
- 251 • Furthermore, there are hotspots of numbers of eddies in other regions of the ocean,
 252 such as boundary currents and the Antarctic Circumpolar Current.
- 253 • An interesting feature shown in both datasets is a predominant patchiness where
 254 the count of the eddies is much larger. These puzzling pattern remains unknown.
 255 Although it looks like a propagation pattern, it could be that eddies persist for
 256 longer in those areas.



234 **Figure 4.** Hemispherical seasonality of eddy kinetic energy (EKE), coherent eddy kinetic en-
 235 ergy (CEKE). Panels a, and b show the northern hemisphere seasonal cycle, while panels c, and
 236 d correspond to the southern hemisphere. Dashed lines correspond to the seasonal cycle of the
 237 fields and dotted lines show the seasonal cycle of the wind magnitude smoothed over 120 days
 238 (moving average). The green and magenta stars show the maximum of the seasonal cycle for the
 239 kinetic energy components and the wind magnitude, respectively. The line colors show the year.

- The eddy amplitude as expected is maximum at the boundary currents and hotspots in the southern ocean.
- Interior of the gyres we can observe that there is an important amplitude of the coherent eddy field.
- Preferred eddy amplitude sign in boundary currents; positive amplitude polewards to the boundary current mean location, and negative amplitude equatorwards. This is consistent with the shed of coherent eddies from the boundary currents.
- There regions with large CEKE ratio show also a large coherent eddy amplitude.
- Absolute eddy amplitude has the similar signature as CEKE.

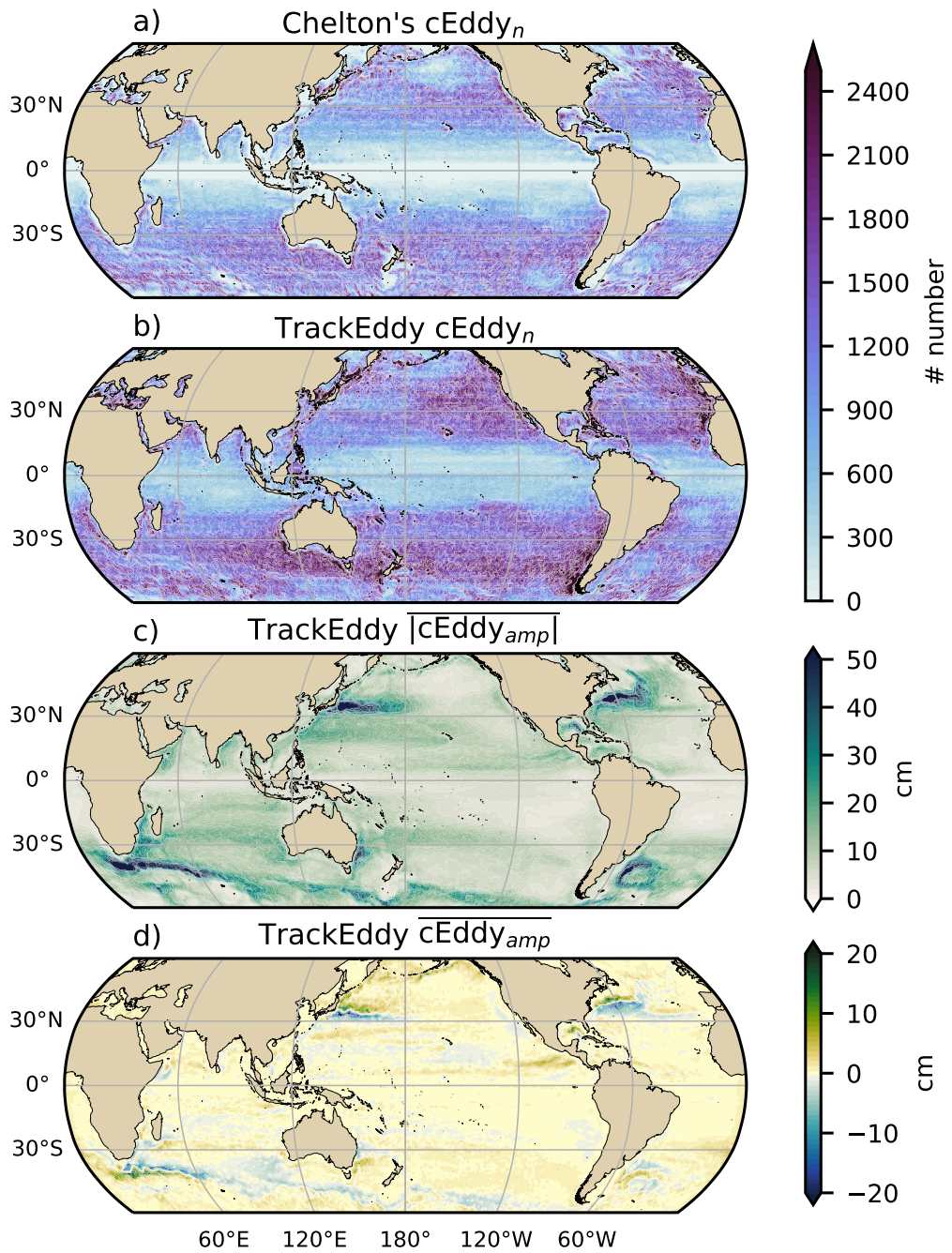
4.0.1 Seasonality

Figure 6

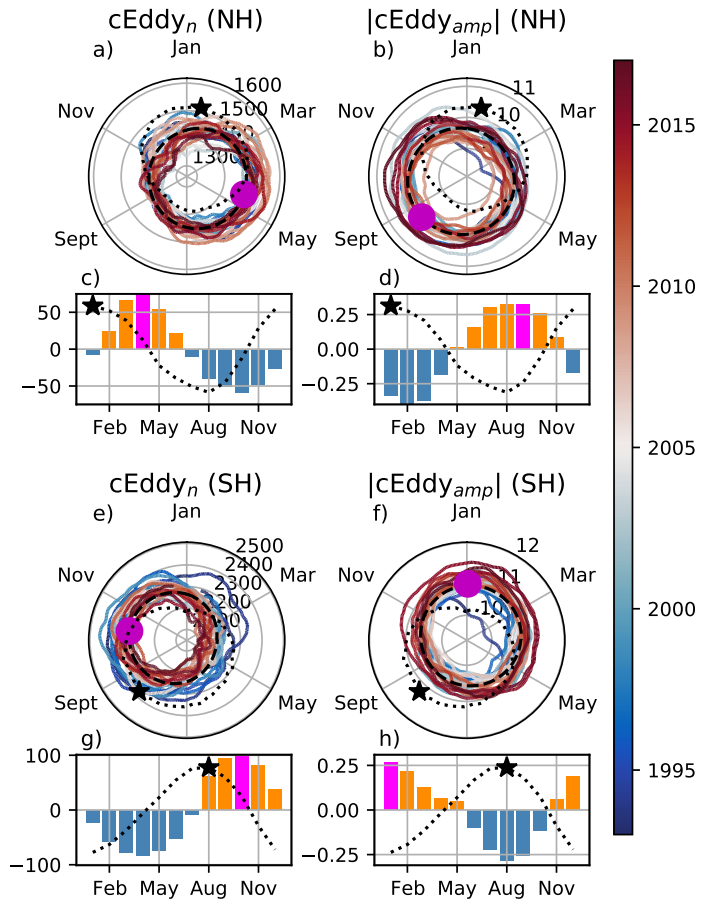
- Seasonality of the number of eddies in the Northern Hemisphere peaks on May, while the Southern Hemisphere peaks on October.
- The seasonality of the amplitude of the eddies is consistent with those of the Coherent eddy kinetic energy.
- Interestingly, there is a 3 month lag between the winds and the seasonality of the number of eddies, while the eddy amplitude responds approximately 6 months after the maximum winds.
- Note that both coherent eddy amplitudes seem to peak around the same time.
- If we look closely, the growing-shrinking concentric circles correspond to an increasing-decreasing trend. These are particularly obvious as a decrease in the eddy number in the Southern Hemisphere, and an increase in the eddy amplitude.
- Coherent eddy radius also peaks in the same months of the amplitude with scales of 100km diameters.

Should I add a seasonal cycle of the eddy radius? eddy area?, I've plotted it follows closely the eddy amplitude, which is expected, but as I just argued, the mean seasonal cycle shows on average a peak in summertime with diameters of 90 km, in fact, if I mask the radius with eddies larger than 90km, the seasonal cycle peaks in October, while eddies smaller than 90km peak on May.

Figure 6



266 **Figure 5.** Climatology of the coherent eddy statistics. a) Climatology of the number of coher-
 267 ent eddies ($cEddy_n$) identified by Chelton et al. (2007); b) Climatology of the number of coher-
 268 ent eddies ($cEddy_n$) identified by Martínez-Moreno et al. (2019); c) Climatology of the mean abso-
 269 lute coherent eddy amplitude ($cEddy_{amp}$). d) Climatology of the mean coherent eddy amplitude
 270 ($cEddy_{amp}$).



286 **Figure 6.** Hemispherical seasonality of the coherent eddy statistics; a,e) seasonal cycle of the
 287 number of coherent eddies ($cEddy_n$); b,f) seasonal cycle of the mean coherent eddy amplitude
 288 ($cEddy_{amp}$); c,g) seasonal cycle of the warm core coherent eddies amplitude (positive $cEddy_{amp}$);
 289 d,h) seasonal cycle of the cold core coherent eddies amplitude (negative $cEddy_{amp}$). Panels a,b
 290 and c show the northern hemisphere seasonal cycle, while panels d,e, and f correspond to the
 291 southern hemisphere. Dashed lines correspond to the seasonal cycle of the fields and dotted lines
 292 show the seasonal cycle of the wind magnitude smoothed over 120 days (moving average). The
 293 green and magenta stars show the maximum of the seasonal cycle for each field and the wind
 294 magnitude, respectively. The line colors show the year.

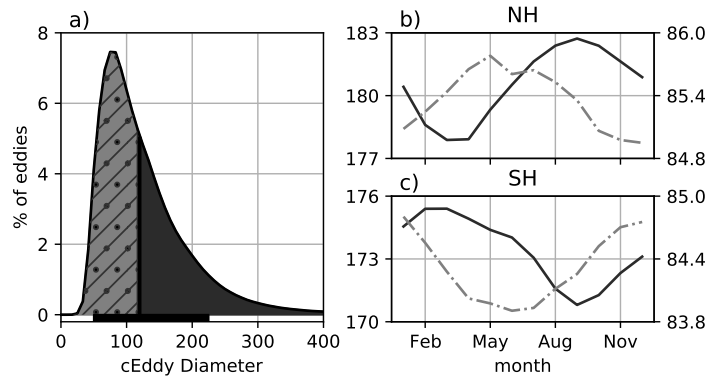


Figure 7. Hemispherical seasonality of the coherent eddy diameter

295

- a

302

5 Trends

312

Figure 13

314

- The number and amplitude of coherent eddies from two eddy tracking algorithms show consistent trend patterns.
- In particular, we observe a decrease in the number of eddies in the southern ocean, as well as sectors in the North Atlantic and North Pacific.
- Meanwhile the amplitude seems to be increasing in those same regions.
- Some of these regions have undergone a readjustment to stronger winds, thus the observed trends in the eddy amplitude suggests an intensification of the coherent eddy field to an increase in the forcing.
- This increase is consistent with Martínez-Moreno et al. (2021)

315

316

317

318

319

320

321

322

329

6 Regional

330

6.1 Boundary Currents

331

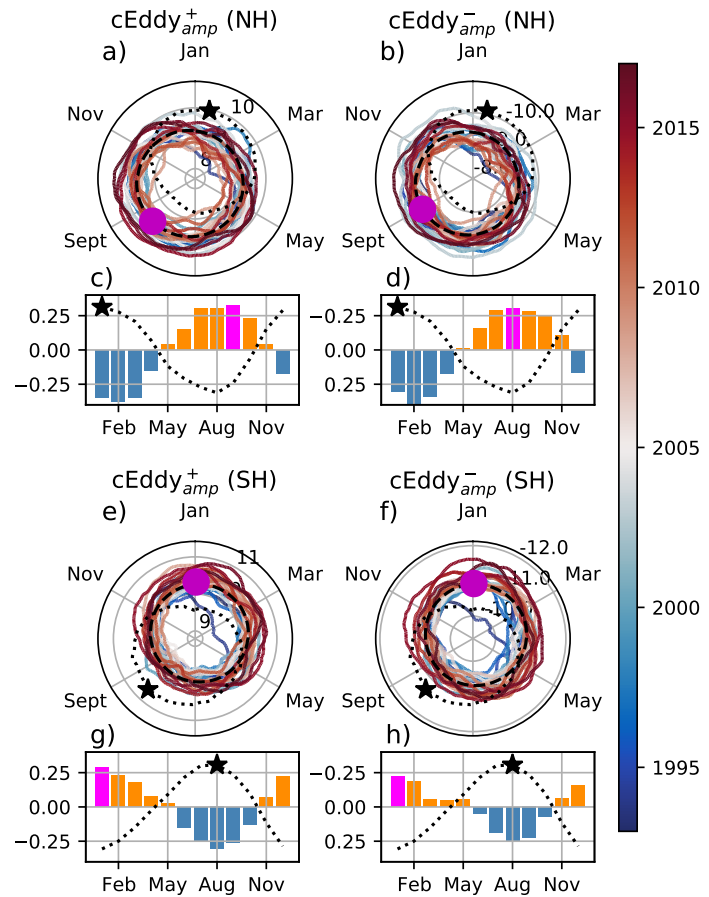
Figure 10

332

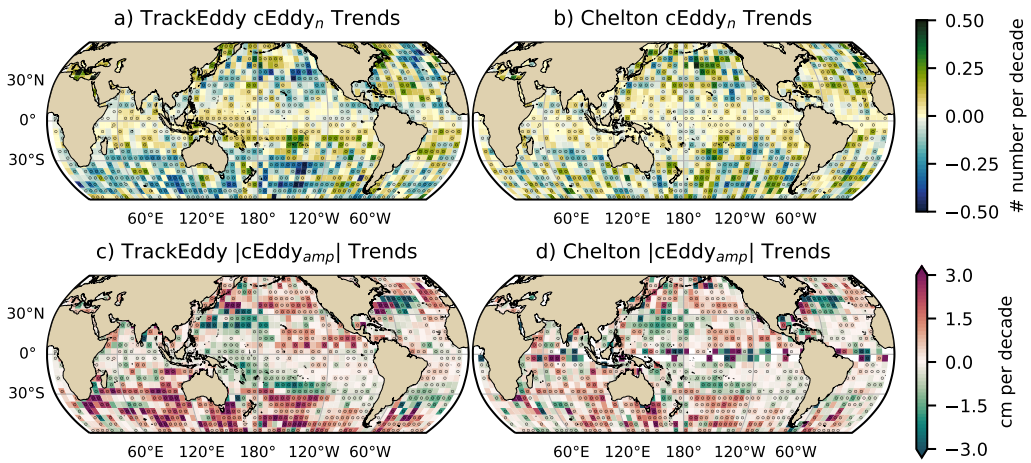
- Described similar to figure 7, 8, and 9
- Note that boundary currents have a consistent seasonal cycle in the positive and negative eddy amplitude.

333

334



303 **Figure 8.** Hemispherical seasonality of the coherent eddy statistics; a,e) seasonal cycle of the
 304 number of coherent eddies ($cEddy_n$); b,f) seasonal cycle of the mean coherent eddy amplitude
 305 ($cEddy_{amp}$); c,g) seasonal cycle of the warm core coherent eddies amplitude (positive $cEddy_{amp}$);
 306 d,h) seasonal cycle of the cold core coherent eddies amplitude (negative $cEddy_{amp}$). Panels a,b
 307 and c show the northern hemisphere seasonal cycle, while panels d,e, and f correspond to the
 308 southern hemisphere. Dashed lines correspond to the seasonal cycle of the fields and dotted lines
 309 show the seasonal cycle of the wind magnitude smoothed over 120 days (moving average). The
 310 green and magenta stars show the maximum of the seasonal cycle for each field and the wind
 311 magnitude, respectively. The line colors show the year.



323 **Figure 9.** Trends of coherent eddy statistics. a) and b) Trends of the number of identified
 324 coherent eddies from satellite observations identified using TrackEddy, and those reported in
 325 Chelton's dataset. c) and e) Trends of the mean absolute value of identified coherent eddies am-
 326 plitude from satellite observations identified using TrackEddy, and those reported in Chelton's
 327 dataset. Gray stippling shows regions that are statistically significant above the 95% confidence
 328 level.

- As expected, the seasonal cycle is opposite to BC in the northern hemisphere.

337 **Figure 11**

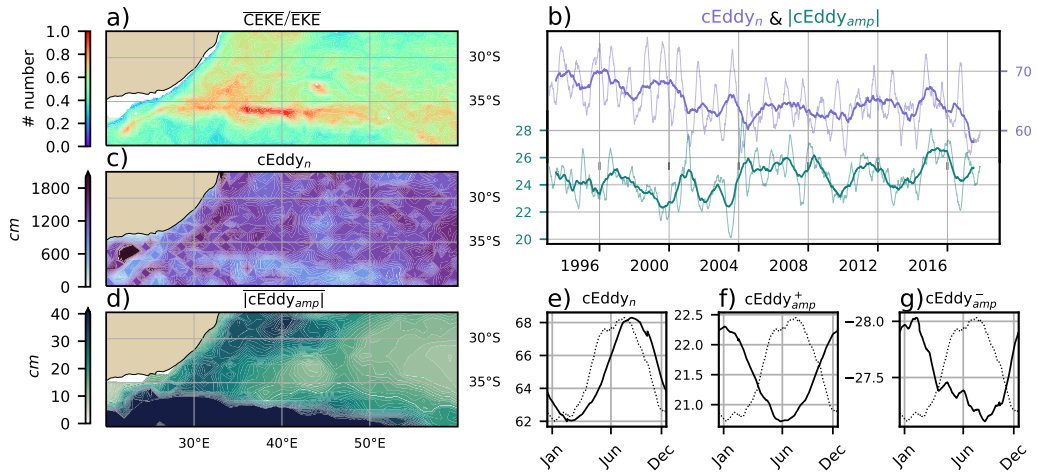
- Described similar to figure 7, 8, and 9
- Note that boundary currents have a consistent seasonal cycle in the positive and negative eddy amplitude.

342 **Figure 12**

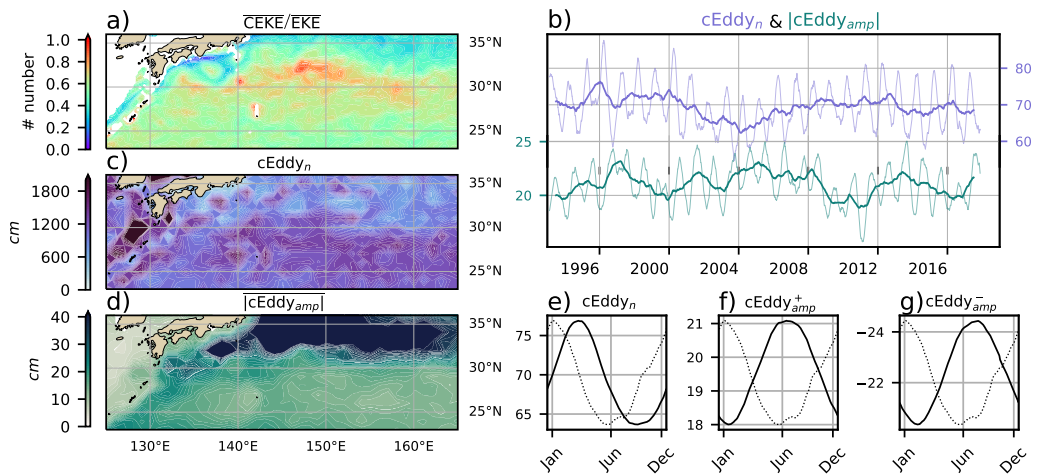
- Described similar to figure 7, 8, and 9
- Note that boundary currents have a consistent seasonal cycle in the positive and negative eddy amplitude.
- Delete Fig 11 or 12, they are really similar. What do you think?

348 **6.2 Eastern currents**

349 **Figure 7**



336

Figure 10. Same as Figure 13 but for the Agulhas Current.

341

Figure 11. Same as Figure 13 but for the Kuroshio Current.

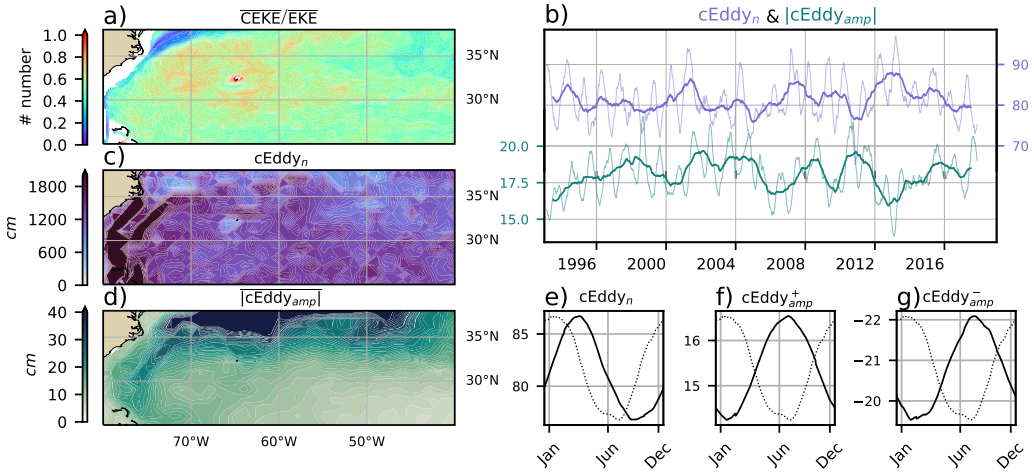
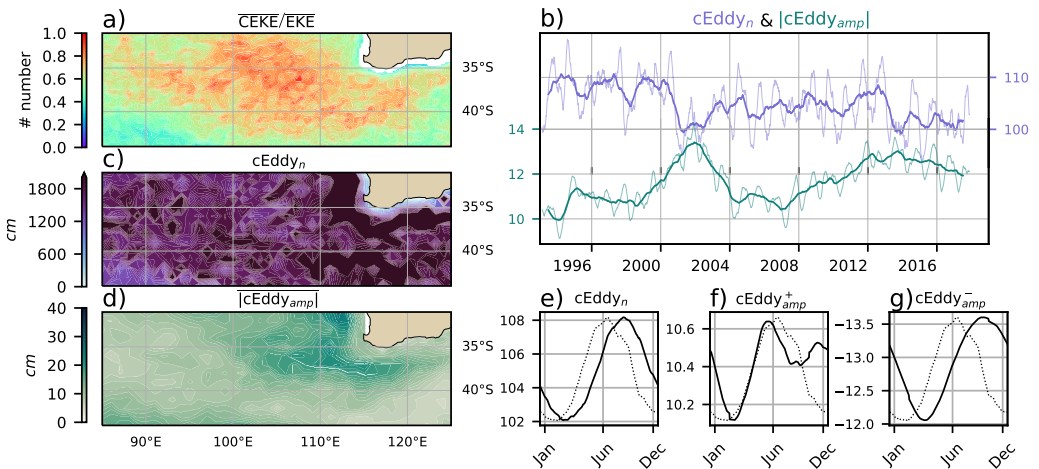


Figure 12. Move to supplementary Same as Figure 13 but for the Gulf Stream.

- South of the Leeuwin Current there is an important dominance fo the coherent eddy field, where it explains around 80% of the eddy kinetic energy.
- Although this region does not have a large EKE, we can observe a considerable amount of eddies across the region, but more importantly the coherent eddy amplitude is particularly large in those regions with coherent eddy dominance.
- The solid lines show an decrease in the number of eddies, but an increase in the eddy amplitude.
- Moreover, the coherent eddy number peaks in August.
- Meanwhile coherent eddies with the positive amplitude have a smaller amplitude than the negative, furthermore, the positive eddies peak in Jun and show a inter-annual modulation, while the negative eddies peak in October.
- Research regional dynamics (Add here why we may expect this response.)

Figure 9

- Here we observe that the number of eddies and eddy amplitude are large in the area where the coherent eddies dominate the eddy field.
- Dynamically, in this region eddies are generated due to Rossby wave propagation along the coast that becomes unstable and sheds eddies at the Tehuantepec Gulf.
- The seasonal cycle shows a peak in Jun, while the positive amplitude is observed in March and the negative amplitude maximum occurs in September.



362 **Figure 13.** Climatology of the eddy field and coherent eddy field at the Leeuwin Current. a)
 363 Ratio of mean coherent eddy kinetic energy ($\overline{\text{CEKE}}$) versus mean eddy kinetic energy ($\overline{\text{EKE}}$); b)
 364 Thick lines show the running average over 2 years and thin lines show the running average over
 365 90 days of the coherent eddy number sum and the average absolute coherent eddy amplitude; c)
 366 Map of the number of eddies; d) Map of the average absolute coherent eddy amplitude; e) Sea-
 367 sonal cycle of the number of eddies f) Seasonal cycle of the positive coherent eddy amplitude. g)
 368 Seasonal cycle of the negative coherent eddy amplitude.

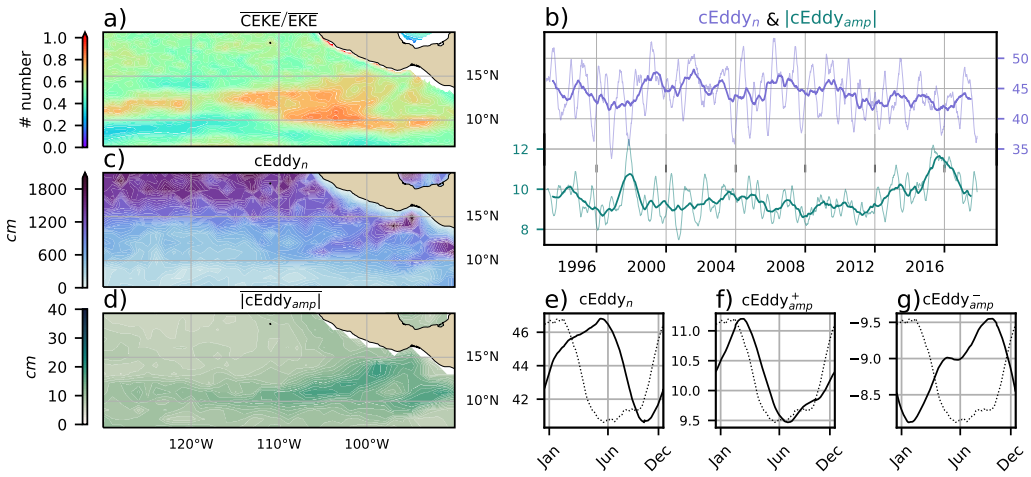


Figure 14. Same as Figure 13 but for the East Tropical Pacific.

377

- Research regional dynamics (Add here why we may expect this response.)

378

7 Summary and Conclusions

379

Acknowledgments

380

Chelton & Schlax (2013) dataset was produced by SSALTO/DUACS and distributed by AVISO+ (<https://www.aviso.altimetry.fr/>) with support from CNES, developed and validated in collaboration with E.Mason at IMEDEA. Global coherent eddy reconstruction, coherent and non-coherent eddy kinetic energy datasets, in addition to gridded coherent eddy tracking datasets are publicly available at (<https://doi.org/10.5281/zenodo.4646429>). All analyses and figures in this manuscript are reproducible via Jupyter notebooks and instructions can be found in the Github repository `CEKE_climatology` (https://github.com/josuemtzmo/CEKE_climatology). Trends used the Python Package `xarrayMannKendall` (<https://doi.org/10.5281/zenodo.4458776>)

389

References

390

- Arbic, B. K., Polzin, K. L., Scott, R. B., Richman, J. G., & Shriver, J. F. (2013). On Eddy Viscosity, Energy Cascades, and the Horizontal Resolution of Gridded Satellite Altimeter Products*. *Journal of Physical Oceanography*, 43(2), 283–300. doi: 10.1175/jpo-d-11-0240.1

- 394 Ashkezari, M. D., Hill, C. N., Follett, C. N., Forget, G., & Follows, M. J. (2016).
 395 Oceanic eddy detection and lifetime forecast using machine learning methods.
 396 *Geophysical Research Letters*, 43(23). doi: 10.1002/2016gl071269
- 397 Beron-Vera, F. J., Wang, Y., Olascoaga, M. J., Goni, G. J., & Haller, G. (2013). Ob-
 398 jective Detection of Oceanic Eddies and the Agulhas Leakage. *Journal of Physical*
 399 *Oceanography*, 43(7), 1426–1438. doi: 10.1175/JPO-D-12-0171.1
- 400 Bouali, M., Sato, O. T., & Polito, P. S. (2017). Temporal trends in sea surface tem-
 401 perature gradients in the South Atlantic Ocean. *Remote Sensing of Environment*,
 402 194, 100–114. doi: 10.1016/j.rse.2017.03.008
- 403 Callies, J., Flierl, G., Ferrari, R., & Fox-Kemper, B. (2015). The role of mixed-layer
 404 instabilities in submesoscale turbulence. *Journal of Fluid Mechanics*, 788, 5–41.
 405 doi: 10.1017/jfm.2015.700
- 406 Cane, M. A., Clement, A. C., Kaplan, A., Kushnir, Y., Pozdnyakov, D., Seager, R.,
 407 ... Murtugudde, R. (1997). Twentieth-Century Sea Surface Temperature Trends.
 408 *Science*, 275(5302), 957–960. doi: 10.1126/science.275.5302.957
- 409 Chelton, D. B., Gaube, P., Schlax, M. G., Early, J. J., & Samelson, R. M. (2011).
 410 The influence of nonlinear mesoscale eddies on near-surface oceanic chlorophyll.
 411 *Science*, 334(6054), 328–32. doi: 10.1126/science.1208897
- 412 Chelton, D. B., & Schlax, M. G. (2013). *Mesoscale eddies in altimeter observations*
 413 *of ssh*.
- 414 Chelton, D. B., Schlax, M. G., Samelson, R. M., & de Szoeke, R. A. (2007). Global
 415 observations of large oceanic eddies. *Geophysical Research Letters*, 34(15),
 416 L15606. doi: 10.1029/2007GL030812
- 417 CMEMS. (2017). The Ssalto/Duacs altimeter products were produced and dis-
 418 tributed by the Copernicus Marine and Environment Monitoring Service. *Aviso*
 419 *Dataset*. Retrieved from <https://www.aviso.altimetry.fr/>
- 420 Cui, W., Wang, W., Zhang, J., & Yang, J. (2020). Identification and census statis-
 421 tics of multicore eddies based on sea surface height data in global oceans. *Acta*
 422 *Oceanologica Sinica*, 39(1), 41–51. doi: 10.1007/s13131-019-1519-y
- 423 Faghmous, J. H., Frenger, I., Yao, Y., Warmka, R., Lindell, A., & Kumar, V. (2015,
 424 6). A daily global mesoscale ocean eddy dataset from satellite altimetry. *Scientific*
 425 *Data*, 2, 150028 EP -. doi: 10.1038/sdata.2015.28
- 426 Ferrari, R., & Wunsch, C. (2009). Ocean Circulation Kinetic Energy: Reservoirs,

- 427 Sources, and Sinks. *Annual Review of Fluid Mechanics*, 41(1), 253–282. doi: 10
428 .1146/annurev.fluid.40.111406.102139
- 429 Frenger, I., Gruber, N., Knutti, R., & Münnich, M. (2013). Imprint of Southern
430 Ocean eddies on winds, clouds and rainfall. *Nature Geoscience*, 6(8), 608 EP -.
431 doi: 10.1038/ngeo1863
- 432 Frenger, I., Münnich, M., Gruber, N., & Knutti, R. (2015). Southern Ocean eddy
433 phenomenology. *Journal of Geophysical Research: Oceans*, 120(11), 7413-7449.
434 doi: 10.1002/2015JC011047
- 435 Fu, L., Chelton, D., Le Traon, P., & Oceanography, M. R. (2010). Eddy dynamics
436 from satellite altimetry. *Oceanography*, 23(4), 14-25. doi: 10.2307/24860859
- 437 Gill, A., Green, J., & Simmons, A. (1974). Energy partition in the large-scale ocean
438 circulation and the production of mid-ocean eddies. *Deep Sea Res Oceanogr Abstr*,
439 21(7), 499-528. doi: 10.1016/0011-7471(74)90010-2
- 440 Hogg, A. M., & Blundell, J. R. (2006). Interdecadal variability of the southern
441 ocean. *Journal of Physical Oceanography*, 36(8), 1626-1645. doi: 10.1175/
442 JPO2934.1
- 443 Hogg, A. M., Meredith, M. P., Chambers, D. P., Abrahamsen, E. P., Hughes,
444 C. W., & Morrison, A. K. (2015). Recent trends in the Southern Ocean
445 eddy field. *Journal of Geophysical Research: Oceans*, 120(1), 257-267. doi:
446 10.1002/2014JC010470
- 447 Hu, S., Sprintall, J., Guan, C., McPhaden, M. J., Wang, F., Hu, D., & Cai,
448 W. (2020, 2). Deep-reaching acceleration of global mean ocean circula-
449 tion over the past two decades. *Science Advances*, 6(6), eaax7727. doi:
450 10.1126/sciadv.aax7727
- 451 Japan Meteorological Agency, Japan. (2013). *Jra-55: Japanese 55-year reanalysis,*
452 *daily 3-hourly and 6-hourly data.* Boulder CO: Research Data Archive at the Na-
453 tional Center for Atmospheric Research, Computational and Information Systems
454 Laboratory. Retrieved from <https://doi.org/10.5065/D6HH6H41>
- 455 Kang, D., & Curchitser, E. N. (2017). On the Evaluation of Seasonal Variability of
456 the Ocean Kinetic Energy. *Geophysical Research Letters*, 47, 1675-1583. doi: 10
457 .1175/JPO-D-17-0063.1
- 458 Li, G., Cheng, L., Zhu, J., Trenberth, K. E., Mann, M. E., & Abraham, J. P. (2020).
459 Increasing ocean stratification over the past half-century. *Nature Climate Change*,

- 460 1–8. doi: 10.1038/s41558-020-00918-2
- 461 Martínez-Moreno, J., Hogg, A. M., England, M., Constantinou, N. C., Kiss, A. E.,
462 & Morrison, A. K. (2021). Global changes in oceanic mesoscale currents over the
463 satellite altimetry record. *Journal of Advances in Modeling Earth Systems*, 0(ja).
464 doi: 10.1029/2019MS001769
- 465 Martínez-Moreno, J., Hogg, A. M., Kiss, A. E., Constantinou, N. C., & Morrison,
466 A. K. (2019). Kinetic energy of eddy-like features from sea surface altimeter.
467 *Journal of Advances in Modeling Earth Systems*, 11(10), 3090–3105. doi:
468 10.1029/2019MS001769
- 469 Patel, R. S., Llort, J., Strutton, P. G., Phillips, H. E., Moreau, S., Pardo, P. C.,
470 & Lenton, A. (2020). The Biogeochemical Structure of Southern Ocean
471 Mesoscale Eddies. *Journal of Geophysical Research: Oceans*, 125(8). doi:
472 10.1029/2020jc016115
- 473 Pilo, G. S., Mata, M. M., & Azevedo, J. L. L. (2015). Eddy surface properties and
474 propagation at Southern Hemisphere western boundary current systems. *Ocean
475 Science*, 11(4), 629–641. doi: 10.5194/os-11-629-2015
- 476 Qiu, B. (1999). Seasonal Eddy Field Modulation of the North Pacific Subtropical
477 Countercurrent: TOPEX/Poseidon Observations and Theory. *Journal of Physical
478 Oceanography*, 29(10), 2471–2486. doi: 10.1175/1520-0485(1999)029<2471:sefmot>2
479 .0.co;2
- 480 Qiu, B., & Chen, S. (2004). Seasonal Modulations in the Eddy Field of the South
481 Pacific Ocean. *Journal of Physical Oceanography*, 34(7), 1515–1527. doi: 10.1175/
482 1520-0485(2004)034<1515:smitef>2.0.co;2
- 483 Qiu, B., Chen, S., Klein, P., Sasaki, H., & Sasai, Y. (2014). Seasonal Mesoscale
484 and Submesoscale Eddy Variability along the North Pacific Subtropical Coun-
485 tercurrent. *Journal of Physical Oceanography*, 44(12), 3079–3098. doi:
486 10.1175/JPO-D-14-0071.1
- 487 Ruela, R., Sousa, M. C., deCastro, M., & Dias, J. M. (2020). Global and regional
488 evolution of sea surface temperature under climate change. *Global and Planetary
489 Change*, 190, 103190. doi: 10.1016/j.gloplacha.2020.103190
- 490 Sasaki, H., Klein, P., Qiu, B., & Sasai, Y. (2014). Impact of oceanic-scale inter-
491 actions on the seasonal modulation of ocean dynamics by the atmosphere. *Nature
492 Communications*, 5(1), 5636. doi: 10.1038/ncomms6636

- 493 Schubert, R., Schwarzkopf, F. U., Baschek, B., & Biastoch, A. (2019). Submesoscale
494 Impacts on Mesoscale Agulhas Dynamics. *Journal of Advances in Modeling Earth*
495 *Systems*, 11(8), 2745–2767. doi: 10.1029/2019ms001724
- 496 Siegel, D., Peterson, P., DJ, M., Maritorena, S., & Nelson, N. (2011). Bio-optical
497 footprints created by mesoscale eddies in the Sargasso Sea. *Geophysical Research*
498 *Letters*, 38(13), n/a-n/a. doi: 10.1029/2011GL047660
- 499 Uchida, T., Abernathey, R., & Smith, S. (2017). Seasonality of eddy kinetic energy
500 in an eddy permitting global climate model. *Ocean Modelling*, 118, 41-58. doi: 10
501 .1016/j.ocemod.2017.08.006
- 502 Wunsch, C. (2020). Is The Ocean Speeding Up? Ocean Surface Energy Trends.
503 *Journal of Physical Oceanography*, 50(11), 1–45. doi: 10.1175/jpo-d-20-0082.1
- 504 Wunsch, C., & Ferrari, R. (2004). VERTICAL MIXING, ENERGY, AND THE
505 GENERAL CIRCULATION OF THE OCEANS. *Annual Review of Fluid Me-*
506 *chanics*, 36(1), 281–314. doi: 10.1146/annurev.fluid.36.050802.122121
- 507 Wyrtki, K., Magaard, L., & Hager, J. (1976). Eddy energy in the oceans. *Journal of*
508 *Geophysical Research*, 81(15), 2641-2646. doi: 10.1029/JC081i015p02641
- 509 Yue, S., & Wang, C. (2004). The Mann-Kendall Test Modified by Effective Sample
510 Size to Detect Trend in Serially Correlated Hydrological Series. *Water Resources*
511 *Management*, 18(3), 201–218. doi: 10.1023/b:warm.0000043140.61082.60